Spatial Distribution of Precipitation and Heat Fluxes over the North Western Pacific During the Winter Monsoon Season

*Munehisa Yamamoto[1] and Kenji Nakamura[2]
(1: Graduate School of Environmental Studies, Nagoya University,
2: Hydrospheric Atmospheric Research Center, Nagoya University)
* Hydrospheric Atmospheric Research Center, Nagoya University, Japan, 464-8601, Furo-cho, Chikusa Nagoya, Japan. e-mail: s040117d@mbox.nagoya-u.ac.jp

Abstract

Ocean around Japan is well known as the precipitation zone of the winter monsoon. In this region, synoptic scale disturbances cause large changes of precipitation and cloud distributions. Especially, during the cold outbreaks, heat fluxes are important role to form the precipitation. Then, we investigated the spatial characteristics of precipitation and the heat fluxes. In this study, Tropical Rainfall Measuring Mission (TRMM) (Precipitation Radar (PR), TRMM Microwave Imager (TMI), and Visible and Infrared Scanner (VIRS)), the QuikScat SeaWinds, and the National Centers for Environmental Prediction-Department of Energy Atmospheric Model Intercomparison Project (NCEP-DOE AMIP-II) Reanalysis (NCEP2) dataset are used. The analyzed area is 25°–40°N, 115°–180°E.

During the cold outbreak, the height of precipitation reaches around 2 km and precipitation dominates the shallow, isolated, and weak (20 dBZ). Around the extratropical cyclones and fronts, the height of precipitation reaches around 3 km and precipitation is relatively broad and weak. The solid precipitation over the freezing height is a few.

The heat fluxes are calculated using the simple bulk formulas. The cold outbreaks make the sum of sensible and latent heat fluxes possible to reach to about 800 W m^{-2}. The sensible heat flux over the Japan Sea is similar to that over the coastal region in the Pacific Ocean. The contribution of the latent heat flux over the Pacific Ocean is larger than that over the Japan Sea. This is because the difference of the specific humidity between the sea surface and atmosphere over the Pacific Ocean is larger than that over the Japan Sea due to the Kuroshio Current. On the contrary, the region around the extratropical cyclones and fronts, the sensible and the latent heat fluxes are very small. This is because the differences of temperature and specific humidity between the sea surface and the atmosphere are small.

Keyword: winter precipitation, vertical structure, TRMM.

1. Introduction

Over the mid-latitude oceans, especially northwestern Pacific and north Atlantic area have large amount of precipitation second to the intertropical convergence zone (ITCZ) (e.g. Fig. 4 in Huffman et al. 1997). These areas are also well known as the "storm track", which is the area where many extratropical cyclones move. The cyclone is a source of the heat and moisture supplies over mid latitude area so that it is important to understand the precipitation system around the area. Theoretical and observational studies have done over the Atlantic area, such as the Experiment on Rapidly Intensifying Cyclones over the Atlantic (ERICA) (Hadlock and Kreitzberg 1988) and Fronts and Atlantic Storm Track Experiment (FASTEX) (Joly et al. 1997), and so on. Contrary, there are few observational studies over the Pacific region especially in winter.

The Tropical Rainfall Measurement Mission (TRMM) satellite carries the Precipitation Radar (PR), the Microwave Radiometer (TMI), and the Visible Infrared Scanner (VIRS), which enable to directly measure the horizontal and vertical distribution of precipitation. Kodama and Tamaoki (2002) investigated the climatology of vertical characteristics of winter precipitation over the northwestern Pacific area (c.f. similar analysis in spring and summer shown in by in Fu and Liu (2003)). They suggested from the vertical structure of precipitation observed by PR that shallow stratiform and convective precipitation largely contributed to the total precipitation amount along this area. However, more process studies are needed to know further characteristics or mechanisms. Therefore we focused on the dominant precipitation systems and compared these precipitation characteristics by the TRMM-PR and TMI data.

2. Data

In this study, TRMM-PR, TMI, VIRS, the QuikScat SeaWinds (QSCAT), and NCEP-DOE AMIP-II Reanalysis (NCEP2) dataset (Kanamitsu et al. 2002) are used. The period is during 5 winter seasons (1999/2000–2003/04 December–January–February). Analyzed area is over 25°–40°N and 115°–180°E which covers the area of Japan, the Japan Sea, the Yellow Sea, and the north western Pacific Ocean (Fig. 1).

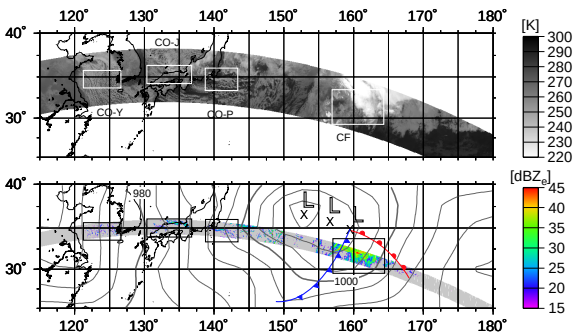

Fig. 1: Spatial distributions of (a) GMS-IR image, (b) SST, (c) divergence (contoured only negative values) with wind vector (arrow), (d) sensible heat flux and (e) latent heat flux. On (d) and (e) positive value indicates color contour and negative value indicates contour line.

We used only the nadir ± 5 angle bins of the PR swath. This corresponds to ≃500 m free cutter level. Because the frequency of echo top height dominates ≃2 km ASL over the north western Pacific region in winter (Kodama and Tamaoki 2002), PR does not well observe precipitation precisely on the edge of swath due to surface clutter by about 2 km. The VIRS data are fitted into PR's narrow swath. We made 0.05° × 0.05° datasets for PR and VIRS to fit into the same resolution.

In the PR2A23 algorithm, the FreezH is estimated from the monthly mean SST and a constant lapse rate (6 K km^{-1}) (hereafter FreezH$_{\mathrm{PR2A23}}$). This estimation is in good agreement in the tropic because both intra-month and inter-annual variability is low. However, the spatiotemporal variation of the FreezH over the mid-latitude region is large (Harris et al. 2000). Thus, the FreezH derived from NCEP2 (hereafter "FreezH$_{\mathrm{NCEP2}}$") is newly defined. The FreezH$_{\mathrm{NCEP2}}$ is calculated that the 2.5° × 2.5° NCEP2 temperature and the geopotential height datasets are linear-interpolated spatiotemporally. The cloud top height (CloudH) is also calculated using the IR brightness temperature and the same method of PR2A23 vertical temperature estimation (CloudH$_{\mathrm{SST}}$) and the interpolation using NCEP2 data (CloudH$_{\mathrm{NCEP2}}$). In addition, the BBH was re-calculated by the V-method to remove the restriction that BBH should be within ±1.5 km from the FreezH$_{\mathrm{PR2A23}}$.

3. Results

3.1. Vertical structure of Winter Precipitation

Winter precipitation patterns are subjectively classified with the cloud pattern into the two types; the extratropical cyclone and front (CF) pattern and the cold outbreak (CO) pattern. For the CO pattern, it is furthermore divided into three categories according to regions, that is, over the Japan Sea (CO-J), over the Yellow Sea (CO-Y), and over the Pacific Ocean (CO-P). Figure 1 shows an example in an orbit. The surface chart indicated that an extratropical cyclone located about 34°N and 160°E, and typical surface disturbances appeared over its western side. Over the Japan Sea, clear JPCZ appeared. The classification was enforced by the same method for the all orbits in the analyzed period. The samples for the CO-J and CO-Y pattern are relatively fewer than that of the CO-P and CF pattern because the sampled area is small. However, the samples are enough to analyze in this study.

Figure 2 shows the contoured frequency of altitude diagrams (CFAD) made from PR2A25 Z factor and histograms of the CloudH, the FreezH, the StormH, and the BBH for each pattern. The CFADs indicate the percentages of frequency in every altitudes.

For the CO pattern (Fig. 2a–c), precipitation echoes are centered in 18–22 dBZ (about 0.2–1 mm h^{-1}) below 2 km. The CFADs show the precipitation is relatively weak and its vertical distributions are similar for the CO-J and CO-Y pattern (Fig. 2a, b). These downward decrease characteristics correspond to the convective snow bands with anvil over the Japan Sea, probably due to evaporation (Sakakibara, 1988). The vertical distribution for the CO-P pattern (Fig. 2c) has downward increasing feature compared with the CO-J and CO-Y pattern. We

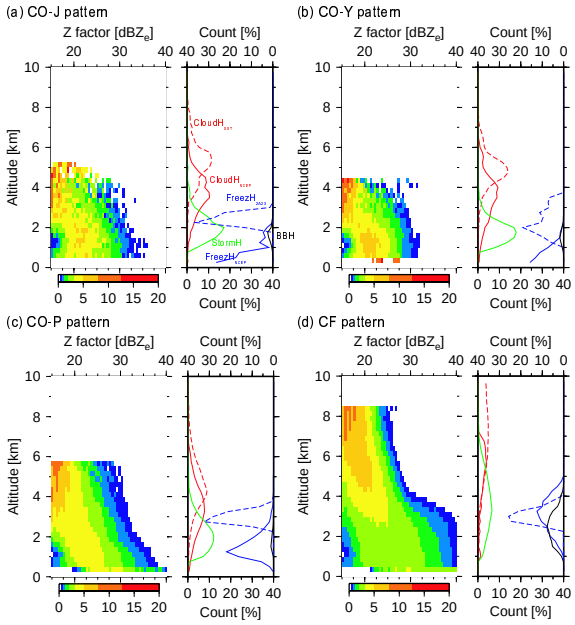

Fig. 2: CFAD (color image) of Ze factor with in the TRMM-PR2A25 product (left panel), and the vertical histograms of the StormH (green line), the CloudH$_{\mathrm{SST}}$ (red dotted line), and the CloudH$_{\mathrm{NCEP2}}$ (red solid line) (right panel with left ordinate). Also plotted are the BBH (black solid line), the FreezH$_{\mathrm{PR2A23}}$ (blue dotted line), and the FreezH$_{\mathrm{NCEP2}}$ (blue solid line) (with right ordinate) in the case of (a) CO-J, (b) CO-Y, (c) CO-P, and (d) CF pattern.

further divided the CO-P pattern into 6 categories by the FreezH$_{\mathrm{NCEP2}}$ every 500 m (FreezH$_{\mathrm{NCEP2}}$ < 1 km) and 250 m (1 km < FreezH$_{\mathrm{NCEP2}}$ < 2.5 km) (not shown). When the FreezH$_{\mathrm{NCEP2}}$ below 1 km, the CFADs are very similar to the CO-J and CO-Y patterns. In the case of 1 km < FreezH$_{\mathrm{NCEP2}}$ < 2 km, the CFADs are similar to whole CO-P pattern (Fig. 2c) because the class of this case is maximum. When the FreezH$_{\mathrm{NCEP2}}$ over 2 km, the CFADs are also similar to those patterns. Compared with FreezH$_{\mathrm{NCEP2}}$, the peak dBZ is ≃1 km, so that it indicates maybe BB. As the FreezH$_{\mathrm{NCEP2}}$ is lower, the peak dBZ is also lower. The downward increase pattern for the CO-P pattern shows due to the BB near the surface.

These characteristics are also shown in the PR2A23 rain type classification (not shown). The percentages of the rain flags of 12, 14, 15 (H-method = stratiform and V-method = others) in PR2A23 for the CO-J, CO-Y, and CO-P pattern are 83.8%, 89.3%, and 76.3%, respectively. This suggests two reasons: 1) the weak precipitation without BB is dominant or 2) the BB detection is failed because the FreezH$_{\mathrm{PR2A23}}$ overestimates compared with FreezH$_{\mathrm{NCEP2}}$. The rain flag of 21 (H-method = convective and V-method = others) which means the convective precipitation cells are included. That of the CO-P and the CO-J patterns are 15.7 % and 6.6 %. These pixels are in the strong precipitation with lightning and convergence zone (e.g. JPCZ). Compared with the CO-J and CO-Y pattern, the CO-P pattern has large percentages of rain flags of 21.

Maximum numbers of the StormH is distributed at 2 km and few echoes reach 4 km. Paying attention to each percentage of StormH / CloudH$_{\mathrm{NCEP2}}$, it is higher in or-

der of the CO-P, CO-Y, and CO-J pattern. It is the same with the distributions of the $\mathrm{FreezH_{NCEP2}}$ and the percentages of warm rain flag. The reason may be because the PR is sensitive for solid precipitation.

For the CF pattern (Fig. 2d), vertical distribution of precipitation echo is downward increasing and its variation is large (20–32 dBZ (0.3–4 mm $\mathrm{h^{-1}}$) near the surface. It means that relatively strong precipitations with fluctuations are included for the CF pattern. The maximum frequency of the StormH appears around 3 km, and some echoes reach to above 6 km and the $\mathrm{CloudH_{NCEP2}}$ distributed around 6 km. The percentage of the stratiform certain flag from PR2A23 is 53.5%. $\mathrm{FreezH_{PR2A23}}$ distributed around 3 km which corresponds to $\mathrm{FreezH_{NCEP2}}$.

3.2. Horizontal scale of Winter Precipitation

In this section, we compare the each precipitation system among the patterns with the horizontal scale. Precipitation intensity (Z factor) increases as the system becomes larger common to all patterns by a certain size (not shown). It is reasonable because the cold air mass supplied the sensible and latent heat from the relatively warm ocean, and the convective clouds grow vertically and horizontally due to the thermal stratification becomes unstable from the bottom as the fetch is longer for the CO pattern. For the CF pattern, large systems contains the active convective region, however, stratiform region with weak precipitation also includes.

Figure 3 shows the prevailing size of each precipitation pattern. The radius of precipitation systems below 10 km dominates for all patterns. However, the CO-P and the CF pattern contain a few percentages larger for medium (r = 10–100 km) and large (r > 100 km) scale of precipitation system than the other patterns. In other words, during the CO, the precipitation systems over the Pacific Ocean are apt to form the larger scale than that over the Japan Sea and the Yellow Sea. For the CF pattern, it is reasonable to form the large scale precipitation around the extratropical cyclone and front.

Most of systems have 2 km stormH, and its aspect ratio is 1–3 common to the CO-J, CO-Y and CO-P pattern. Below 2–3 km, the systems broaden as the stormH is higher. However, above the altitude, the systems narrow rapidly, especially for the CO-J and CO-Y patterns. These characteristics show the precipitation system cannot develop upward due to subsidence of the upper cold air mass. The strength of subsidence appears as the rapid decrease of the aspect ratio. What the larger systems are contained in the CO-P pattern corresponds to the strength of subsidence. We also further classified in some categories by the $\mathrm{FreezH_{NCEP2}}$ for the CO-P pattern as well as the previous section, however, there are no significant different.

For the CF pattern, distributions of pixels are similar to the CO patterns below 2km. However, the aspect ration remains large. It shows that horizontally and vertically large precipitation systems are contained. Especially, the large scale of precipitation systems has more than 3 km stormH.

3.3. Spatial variation in heat fluxes and wind field

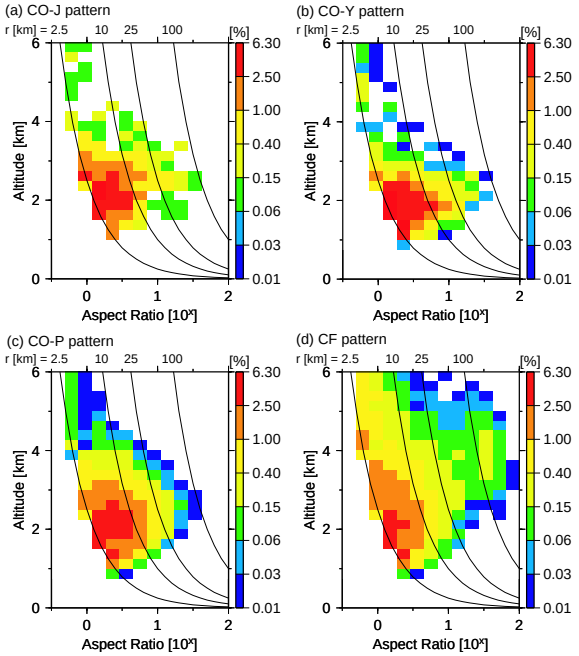

Fig. 3: CFAD (color image) of aspect ratio and radius of precipitation system (solid lines) in the case of (a) CO-J, (b) CO-Y, (c) CO-P, and (d) CF pattern.

We investigated the spatial variations of heat fluxes from the ocean by the simple bulk method using the fine grid observational data. The sensible and latent heat flux are calculated as follows:

$$H = C_p \cdot \rho \cdot C_H \cdot |U_{1000\ \mathrm{hPa}}| \cdot (T_{\mathrm{SST}} - T_{1000\ \mathrm{hPa}}) \quad (1)$$

$$lE = \lambda \cdot \rho \cdot C_E \cdot |U_{1000\ \mathrm{hPa}}| \cdot (q^*_{\mathrm{SST}} - q_{1000\ \mathrm{hPa}}) \quad (2)$$

$$C_H = C_E = 1.2 \times 10^{-3} \quad (3)$$

where H is the sensible heat flux, C_p, λ and ρ are the specific heat capacity at constant pressure, the latent heat of vaporization that is the function of temperature, and the density of air, respectively. U, T, q are the wind speed, temperature, specific humidity, subscripts SST and 1000 hPa denote the sea surface and 1000 hPa. C_H and C_E are the bulk transfer coefficients for sensible heat and latent heat fluxes. This study simply used the constant value of 1.2×10^{-3}. For SST and wind speed data, SST derived from TMI and QSCAT wind data with 0.25° × 0.25° data are also used. For the temperature and relative humidity, there are no observational data over the ocean besides the remote sensing. Thus, 0.25° × 0.25° dataset is generated by interpolation from NCEP2 with 2.5° × 2.5° data to match other data. QSCAT passes over the analyzed region at 18-21 UTC for morning pass. In order to synchronize the observational time, GMS-IR image, NCEP2 data and surface weather charts at 18 UTC are used. The divergence and vorticity near the surface are also calculated from the QSCAT dataset using a method by Sharp (2002). Although this method is for the early detection of tropical cyclone, it is useful for his purpose. First, divergence and vorticity are calculated by the centered difference operation. These values of divergence are used to see the small scale convergence and divergence field. Vorticity was averaged to detect the extratropical cyclone and front. The spatial scale for averaged vortic-

ity is a 7-pixels (175 km) by 7-pixels box centered on the swath points.

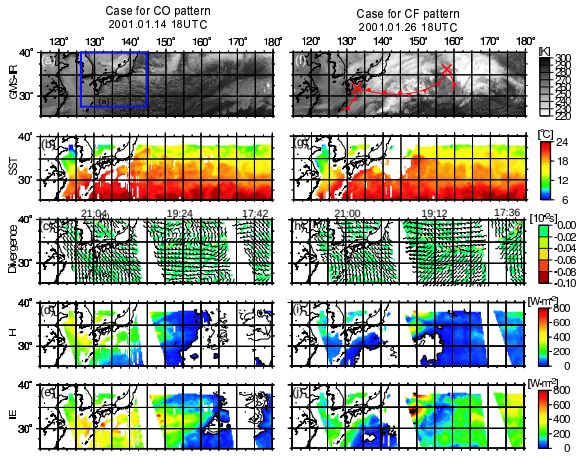

Fig. 4: Spatial distributions of (a, f) GMS-IR image, (b, g) SST, (c, h) divergence (contoured only negative values) with wind vector (arrow), (d, i) sensible heat flux and (e, j) latent heat flux (positive value indicates color contour and negative value indicates contour line) in the case of CO pattern at 18UTC 14th January 2001 (left panel) and the case of CF pattern at 18 UTC 26th January 2001 (right panel).

In this section, we show the two cases for the typical patterns (Fig. 4). One case is on 14 January 2001, when the strong CO appeared (Fig. 4a). The JPCZ was clearly shown in the image of GMS-IR, and the Benald form clouds spread over the Pacific Ocean along the south coast of Japan. These clouds correspond to the convergence area (Fig. 4c). Keep this phenomenon in mind, spatial variations in sensible and latent heat fluxes are described (Fig. 4d, e). From the Japan Sea to the Pacific Ocean, sensible heat flux was high (about 800 W m^{-2}) distributed and weakened southerly. Over the eastern part (160°–), the sensible heat flux is in almost zero or minus. The latent heat flux was strengthened from the base of continent to the southern coast of Japan, and was weakened to the offing from the south coast of Japan, as fetch is longer. It can be explained reasonably. According to meteorological parameters to calculate the heat fluxes, the SST pattern clearly shows the warm Kuroshio Current over the near south coastal zone of Japan (Fig. 4b). Corresponding to location of Kuroshio, ΔT and Δq are also large (about +20 °C, +12 g kg^{-1}, respectively) (not shown). On the contrary, it was dry condition in the atmosphere over the east coast of Japan (35° − 40°N and 150°E) (not shown). Specific humidity was small due to low temperature in condition. As the results of this, the sensible and latent heat fluxes are strengthened.

In 26 January 2001, extratropical cyclones were located at the 32°N and 136°E, and 36°N and 158°E (Fig. 4f). Here, in this case study, the extratropical cyclone at 36°N and 158°E and the warm core over the southern part are focused. From the GMS-IR image in Fig. 4f, high cumulus cloud was observed, corresponding to the cold front along 30°N and 150°E to 33°N and 157°E. There is broad convergence area over this region and relatively strong convergence zone are indicated at the north of extratropical cyclone (Fig. 4h). Over the northern part, the wind was counterclockwise with strong speed. Over the northwestern region of the extratropical cyclone, positive vorticity is strengthened (not shown). The sensible and the latent heat flux was indicated almost zero and minus value (Fig. 4i, j). According to the each meteorological parameter (not shown), under cloud-covered area, ΔT was negative. The relative humidity is near 100 %, and the specific humidity was more than 10 g kg^{-1}. Besides, Δq was near zero at the south of the extratropical cyclone. A series of results shows that the warm and moisture advection was brought from the southwest. While both sensible and latent heat fluxes indicated quite high values around 34°N and 148°E. On the SST distribution (Fig. 4g), relatively warm SST (20°C) is distributed around the 35°N and 150°E, although Kuroshio Current cannot be clearly seen around the south of Tokyo due to the continuous precipitation. In the result, ΔT indicated 10°C over there. Similarly, Δq was also high associated with high SST. In addition, the wind speed was quite strong around the southwest of extratropical cyclone. Such combinative factors leads high sensible and latent heat flux around 34°N and 148°E.

4. Conclusion

Figure 5 shows the schematic diagrams on each pattern of vertical structure with thermodynamic environment on the sea surface. The characteristics which are shallow isolated precipitation are similar among the CO patterns. The heat fluxes have important role to form the pattern. Energy contribution from the surface among the CO patterns is similar, but their partitioning ratio is different. On the contrary, the broad but shallow precipitiation is dominated in the CF pattern. The contribution to the formation and development of precipitation system for the heat fluxes is small.

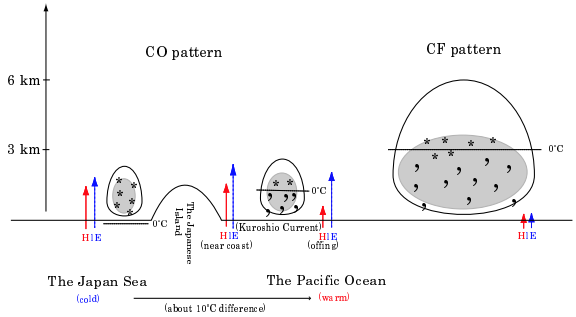

Fig. 5: Schematic illustration of the CF pattern and the CO pattern. But added the effect of lower environments. Cloud area is inside the bold line, gray contoured area and dots are precipitation and its phase (∗; solid precipitation, ı:liquid precipitation)

References

Fu and Liu, *JMSJ*, **81**, 1353-1369, 2003.
Hadlock and Kreitzberg, *BAMS*, **69**, 1309-1320, 1988.
Harris Jr. et al, *JC*, **13**, 4137-4148, 2000.
Huffman et al., *BAMS*, **78**, 5-20, 1997.
Joly et al., *BAMS*, **78**, 1917-1940, 1997.
Kanamitsu et al., *BAMS*, **83**, 1631-1643, 2002.
Kodama and Tamaoki, *JMSJ*, **80**, 1261-1278, 2002.
Sakakibara, *JMSJ*, **66**, 937–953, 1988.
Sharp et al., *BAMS*, **83**, 879–889, 2002.